ISSN 0016-8521, Geotectonics, 2024, Vol. 58, No. 1, pp. 108–127. © Pleiades Publishing, Ltd., 2024.
ISSN 0016-8521, Geotectonics, 2024. © Pleiades Publishing, Ltd., 2024.

Strain Analysis and Microstructural Study of Hamadat Core Complex, Northwestern Arabian Shield, Saudi Arabia

M. H. Al-Hashim[a] and O. M. K. Kassem[b, *]

[a] *King Saud University, Department of Geology and Geophysics, College of Sciences, 11451 Riyadh, Kingdom of Saudi Arabia*

[b] *National Research Center, Department of Geology, Dokki, Cairo, 12622 Egypt*

**e-mail: kassemo1@yahoo.com*

Received June 24, 2023; revised January 24, 2024; accepted February 12, 2024

Abstract—The present work illustrates the structural setting in the Hamadat core complex, which located in the Midyan terrane. It is essential to understand deformational processes and products at different scales, which depend on the calculation of finite strain. To assess the tectonic development and structures in the Hamadat core complex, we use field investigation, finite strain analysis and microstructural examination. The Hamadat core complex employed the Rf/φ and Fry techniques for feldspar and mafic grains with 24 collected samples for gneisses, metavolcano-sedimentary rocks from both the Zaam and Baydah groups, deformed granodiorite for Jar-Salajah intrusion and Qazzaz granite. According to finite-strain data, the various rock units have moderate to high degree of deformation, and the axial ratios for *XZ* section vary from 1.80 to 4.50 for the Rf/φ technique and from 2.10 to 7.40 for the Fry technique. It concluded that the shortening axes display the subvertical related to the subhorizontal foliation. The strain data have the same main-phase foliation and similar deformation behavior. Finite strain acquired through high pressure metamorphism in this instance suggested that the contacts of nappe developed through the buildup of ductile strains. Also, during thrusting and intrusions throughout the deformation process, a building of brittle to ductile deformation was mostly caused by pure shearing in the study area.

Keywords: finite strain, ductile deformation, Hamadat core complex, Saudi Arabia

DOI: 10.1134/S0016852124700079

INTRODUCTION

The major exposures of the Arabian–Nubian Shield are in the Sinai part and Eastern Desert of Egypt, Sudan, Jordan, Eritrea, Saudi Arabia and Yemen. It is made up primarily of low grade metavolcano-sedimentary rocks, with a small amount of ophiolites from the Mozambique Ocean floor. The Mozambique Ocean contains the island arcs, which includes high grade continental rocks in the shield. The northern Arabian–Nubian Shield experienced tectonic expansion between 600 Ma and 550 Ma, which was followed with granitoids in the Arabian–Nubian Shield and the crust heating up overall [13, 21].

The Arabian Shield, which is split into eight areas, was created by the Neoproterozoic basement complex [7, 8, 23, 48, 49] (Fig. 1):

— the Midyan, Hijaz, Asir, and Jiddah terranes in the west-side of the Arabian Shield;

— the Hail, Afif, Ad Dawadimi and Ar Rayn terranes in the east-side of the Arabian Shield.

These terranes are sutures or shear zones that divide the small plates from one another.

The Yanbu belt is impacted by tectonic activity and divides the Midyan and Hijaz areas in the study region [10].

The Ajjaj, Qazzaz and Hamadat shear zones, which locate in the Midyan area, have various features (Fig. 2).

The present region contains the Hamadat complex and Ajjaj shear zone, which represented ~150 km long to 35 km wide. The high grade Hamadat complex was exhumed inside the Ajjaj shear zone from below the intrusive bodies (Nabt, Jar-Salajah, and Imdan) and volcano-sedimentary assemblages (Zaam, Baydah and Al Ays formations) [18, 19].

A variety of approaches have been developed to estimate finite strain, including the Rf/φ [53] and Fry methods [14]. All techniques that use object or point displacement aim to calculate the tectonic strain and changes in the strain ellipse/ellipsoid's form and orientation in 2D and 3D, respectively.

According to research on finite strain, oblate shapes are particularly evident in natural shear zones [16, 25–27, 28, 30, 43]. These oblate shapes can be produced by volume loss for simple shear or by pure

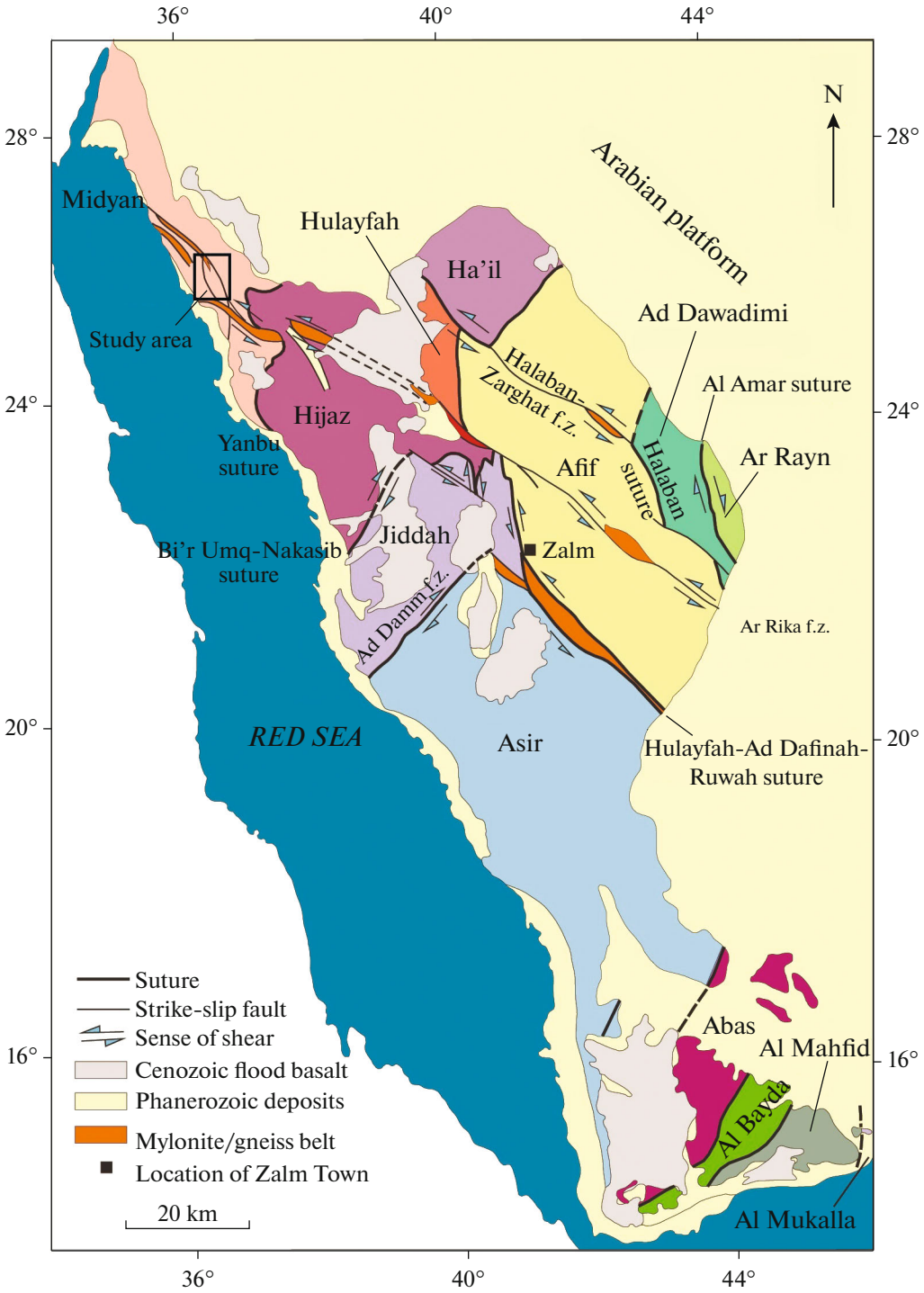

Fig. 1. Geological map of the Arabian Shield, showing different tectonic terrains and sutures (after [20], modified).

shear component preceding shearing with /or without volume loss [46].

The importance of finite strain and the degree of non-coaxiality are assessed for nappe contacts associated with flatling foliation in several orogen internides. Furthermore, strain ratio is identified by recognizing shape ellipsoids and/or division for various rock units that have been deformed [29, 33, 51, 52].

This research has been done on the Hamadat core complex and adjacent area to investigate the microstructure, finite strain, and deformation studies.

The purpose of this study is to provide geological data and tectonic evolution that was gathered from the collected samples and fieldwork. Additionally, we examined the kinematic analysis to identify the type of shear (such as pure shear or/and simple shear) in

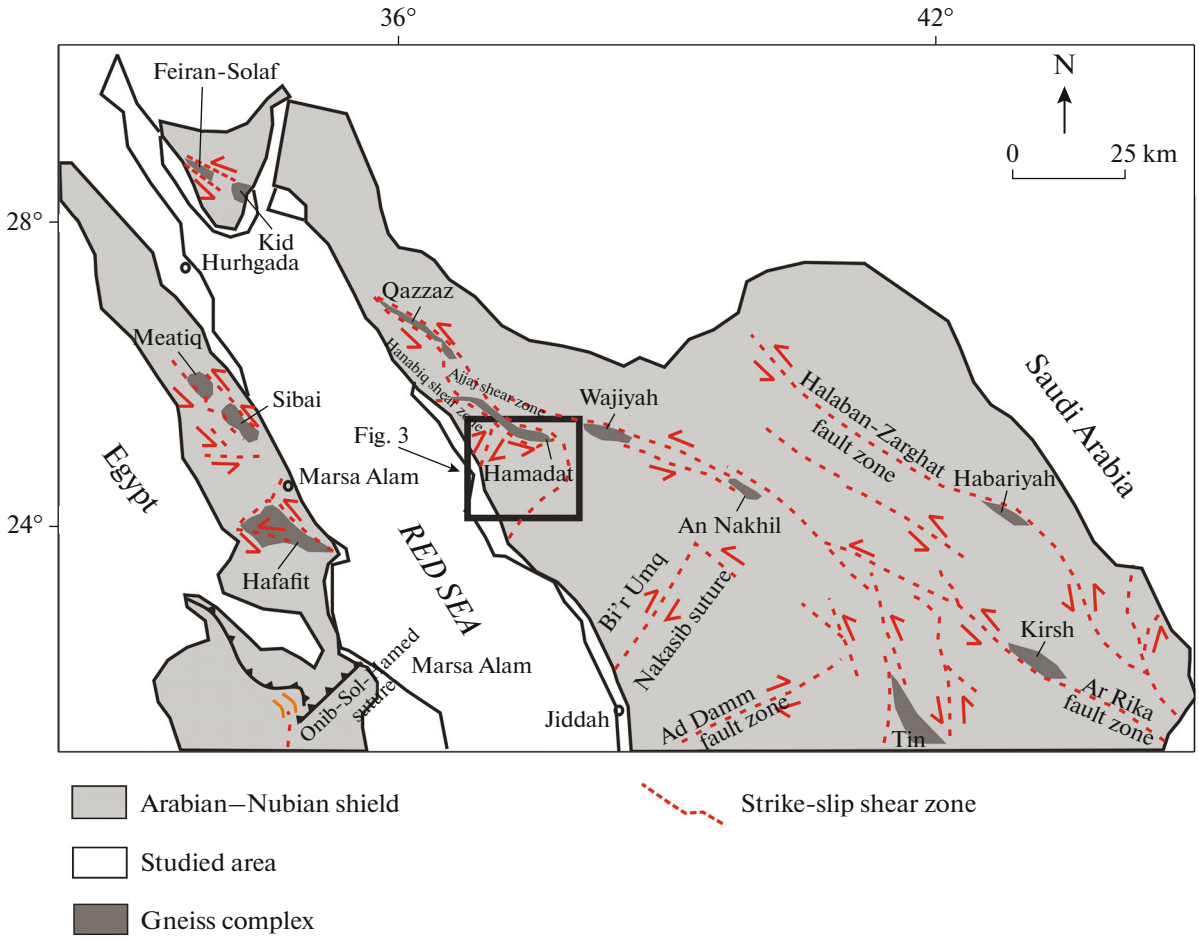

Fig. 2. Overview map of the Najd shear zones and the gneiss complexes in the Arabian–Nubian Shield (after [3], modified).

various deformed rocks. Furthermore, analysis performed clarifies the structures involved post-accretionary thrusting in the Hamadat core complex.

GEOLOGICAL SETTING

Within the Ajjaj shear zone, the Hamadat anticlinorium is considered dome of gneiss and extended 100 km with WNW–ESE trending. According to [15], it comprises of tight folds to the NW and more open folds to the SE. The Ajjaj shear zone cleaved the anticlinorium, which contains both intrusive and metamorphic rocks. In the present region, the metamorphic rocks consist of the Zaam, Bayda and Al Ays groups, which represented the volcanosedimentary rocks (Fig. 3).

These rocks have varying degree of metamorphism and ranging from high grade amphibolite facies to low grade greenschist facies. The Bayda group is distinguished by medium-grade rocks with greenschist facies [3]. Additionally, garnet-bearing gneisses are among the metamorphic rocks. The Hamadat core complex boundary matches with the contact between the high metamorphic rocks (within Hamadat core) and the low-grade rocks (greenschist facies) of the Zaam group (north and south of the Hamadat core), which show parallel to the borders of the Ajjaj shear zone (Fig. 3).

Also, the porphyritic and crystal tuffs have undergone significant crystal-plastic deformation in the highly deformed for Zaam group. This group is comparable volcano-sedimentary successions that can be connected on various map sheets [22].

The intrusive rocks show distinct cross-cutting interactions in Hamadat core complex contain Jar-Salajah batholiths, Nabt intrusion, Qazzaz granite, and Rithmah diorite related to the Ajjaj shear zone [22]. The Jar-Salajah batholiths form tonalite, granodiorite, diorite, trondhjemite, gabbro, and irregular biotite granite bodies.

According to [39], the Nabt intrusion is composed of trondhjemite, tonalite, diorite, and gabbro and intruded the metavolcano-sedimentary rocks to form the Hanabiq branch (Fig. 2).

The majority of Qazzaz granite contains Monzogranite rocks and intruded the Bayda and Al Ays

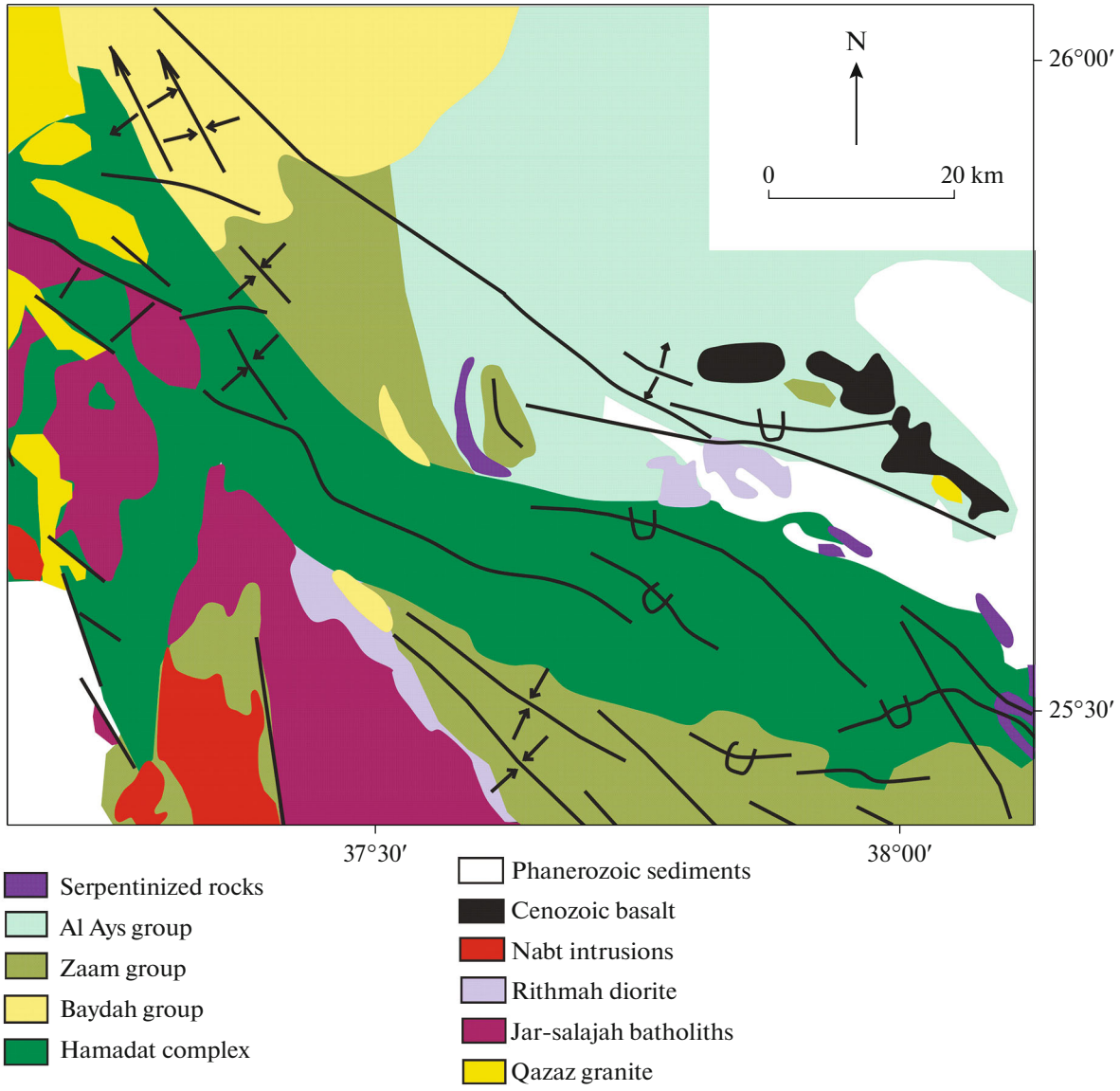

Fig. 3. Lithological map of the Hamadat core complex (after [3], modified).

groups from the east and northern east in the present studied (Fig. 3).

Rithmah intrusion is composed of diorite rocks and found to the east of Jar-Salajah batholiths and the Ajjaj shear zone with various composition and shape. Additionally, various grades of deformation are seen in all of the investigated intrusions. The Hamadat core complex and Ajjaj shear zone contains some undeformed intrusions, whereas other severely deformed rocks nearby exhibit NW–SE shear fabric with parallel to the Ajjaj shear zone.

The deformation implicates the boundary of deformed intrusive massifs and exhibits parallel shear zone. The Nabt intrusion, Jar-Salajah batholiths, Qazzaz granite, and Rithmah diorite are dated between 740 and 620 Ma, usually these structures offer useful geological data to elucidate the history of deformation for present region.

DEFORMATION HISTORY

On the basis of the existence of band structures, the high metamorphism rocks are distinguished by using the enhance LANDSAT images [52] and field observations to create a regional maps of the deformation models [18, 19]. The maps show the direction and strength of foliations that depict the deformation along the Hamadat shear zone (Fig. 4).

The greenschist and amphibolite facies have gradational contacts that are parallel to bedding plane (S0) and almost parallel to the trending (NW–SE) and W–E in the Hamadat shear zone [37].

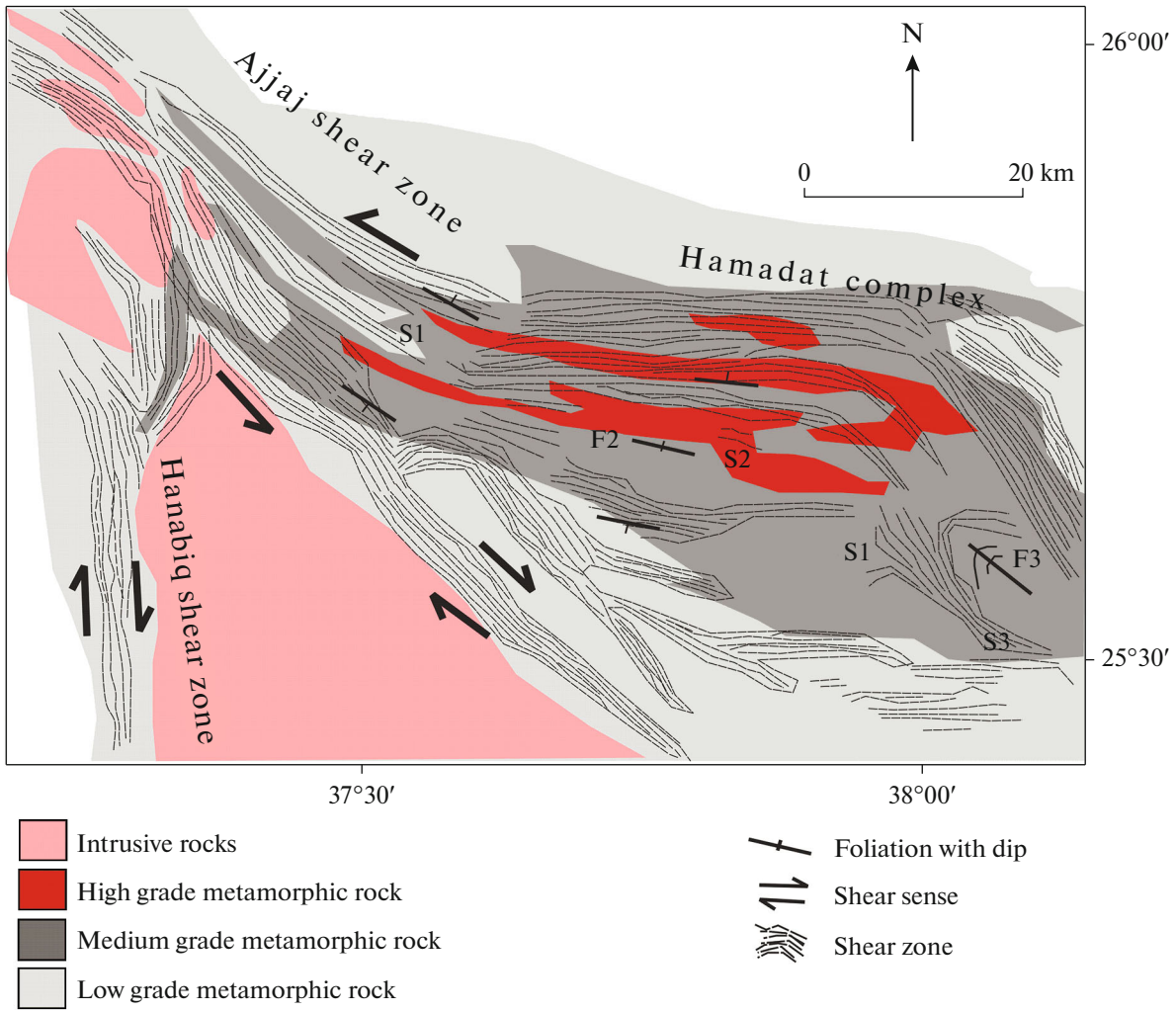

Fig. 4. Deformation pattern and simplified metamorphic map of the Hamadat core complex was derived from field work in combination with enhanced satellite images (after [19]).

Phases of Deformation

It was proposed that four deformation phases (D1–D4) are used to understand the structural components of the studied region [18].

Phase D1. The first deformation phase (D1) formed during the initial foliation (S1). In the Hamadat complex, the foliation (S1) strikes NW–SE with N–E dipping and S–SW with moderate dips, in the northern part and southern part respectively. High-grade metamorphosed rocks have bands that are parallel to (S1).

Phase D2. In second deformation (D2), foliations (S1) were folded and created the foliations (S2), which is parallel to the axial plane of the folds (F2). Folds (F2) exhibit shallow dipping axial surfaces NW–SE trending with the close interlimb angles (Fig. 4).

Phase D3. In the third deformation phase (D3), the Najd fault system is trended into NNW–SSE, which is parallel with various dipping axial surfaces for the open to close folding style of the second folding phase (F3). The second folding phase (F3) changed the foliation (S1) and the first folding phase (F2) axial planes (S2), which is as well related to a third group of foliation (S3) with NNW–SSE trending parallel to the axis of F3 folds. In the eastern side of the Hamadat complex, fold interference patterns that were created in the foliation (S1) by the superposition of folds F2 and F3 are observed (Fig. 4).

Phase D4. The fourth deformation phase (D4) was formed by a mineral lineations (L4) through the shearing. The majority of lineation in the Hamadat complex is located on the foliation planes (S1) and (S2) and sub-horizontal with plunging in the south part. The lineation (L4) follows the WNW–ESE trend of the northern part of Hamadat complex and Ajjaj shear zone. There is a left-lateral shear sense, according to kinematic indications. However, the mineral lineations (L4) occurred in the S1 and S2 planes visible inside the anticlinorium [9].

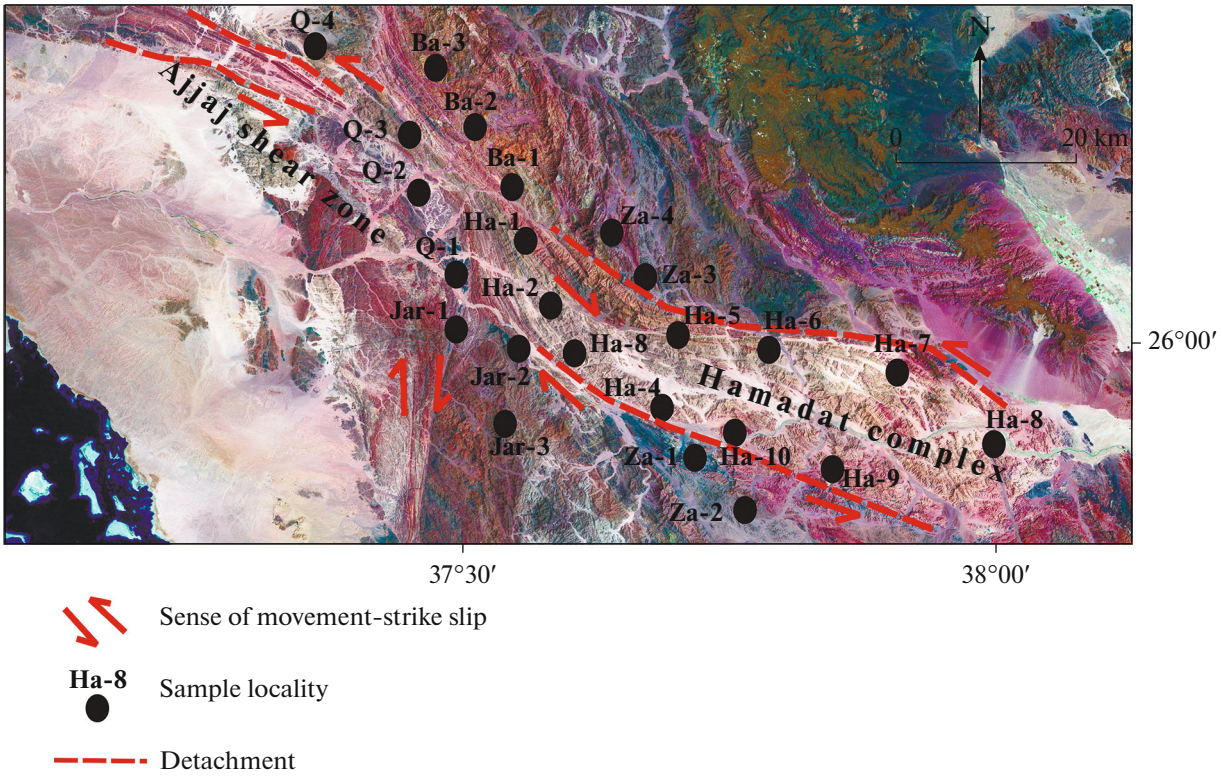

Fig. 5. Landsat map views the sample location and major structural for studied area.

It is crucial to point out that structural components S2, F2, S3, and F3 are too found in displaying distant from the Hamadat anticlinorium.

ANALYTICAL TECHNIQUE

The samples were cut along two perpendicular axis planes known as the *XZ* and *YZ*, which defined the major strain planes [35, 43]. The *XZ* planes are parallel to mineral lineations and perpendicular to foliations, whereas the *YZ* planes are perpendicular to both mineral lineations and foliations [35, 43, 52]. Strain analysis is a mathematical approach for estimating the strain ratios (Rs) using a wide range of strain indicators [40].

Some of the strain factors that are frequently assessed in strain analysis contain strain ratios (Rs), stretching, shortening, and strain ellipsoids for major axes (such as *X*, *Y*, and *Z*, *k* values). Flinn diagram is often utilized to depict the strain ellipsoids shape and indicate deformation types [4, 12, 32].

The Rf/φ and Fry procedures were also utilized to compute the R_{XZ} and R_{YZ} for samples. The minerals individually are digitized for felsic and mafic grains. Strain indicators such as feldspar, quartz, biotite, and hornblende were utilized to evaluate the strain analysis for collected samples. Following that, the outlines were digitized. The long axes and short axes of about 60 grains per section were evaluated on quartz and feldspar grains for Rf/φ analysis, and the average of the aspect ratio for each section was determined in the current study.

The strain for Fry analysis was calculated using the centre points of over 100 quartz, feldspar, biotite, and hornblende per section. Many authors developed and investigated these methodologies, which are critical and widely utilized to determinate strain analysis [17, 24, 34]. In this study, the finite strain (RS_{XZ} and RS_{YZ}) was determined using Ellipse Fit v.3.2.2 software [50], and the "K" values were discovered using Strain Calculator v3.2 software [53].

The 24 samples collected from Hamadat core complex which deal gneisses rocks, metavolcano-sedimentary rocks from both the Zaam and Baydah groups, deformed granodiorite for Jar-Salajah and Qazzaz granite (Fig. 5).

The majority of field samples gathered show NW–SE direction with the modest to steep dip for Hamadat core complex, and these samples were the next (Fig. 5):

— 10 gneisses rocks;

— 4 metavolcano-sedimentary rocks from the Zaam group;

— 3 metavolcano-sedimentary rocks from the Baydah group;

— 3 weakly deformed granodiorite from Qazzaz;

— 4 highly deformed granite from Qazzaz.

These ellipsoids display heterogeneously deformation for varied rocks in order to estimate the finite strain in the Hamadat core complex (Fig. 5).

MICROSTRUCTURAL ANALYSIS

Gneisses rocks, metavolcano-sedimentary rocks from the Zaam and Baydah groups, granodiorite for the Jar-Salajah, and Qazzaz granite make up the Hamadat core complex (Fig. 6a).

They are identified by their dominant slightly SW–NE dipping mylonitic foliation and their gently plunging stretching lineations that run either NW–SE or slightly N–S. The recrystallization of quartz and feldspar were utilized as a guide to assess the metamorphic grade of mylonitization using the microstructure investigation of the study area. Locally, the Hamadat core complex and shear zones underwent varying degrees of metamorphism from greenschist facies to amphibolites-grade metamorphosis. The metavolcano-sedimentary rocks are foliated and sheared in the northwest direction with vertical dipping (Fig. 6b).

The shear zone trending is characterized by various movements with progressively modification of the fold shapes and by open parallel folds at the outer zone to tight flattening at the center (Fig. 6c).

The gneiss rocks in the Hamadat complex have high and medium grades of metamorphism rocks grade.

The extensive recrystallization and metamorphism obscure the intermediate to mafic intrusive and basic tuffaceous or volcanic character of the protoliths of metamorphic rocks [39]. The high grade rocks contain feldspar, quartz, garnet, micas, chlorite, and ilmenite (Fig. 7a).

The foliations are folded and the rock consists of mica, albite, ilmenite, chlorite and biotite. The development biotite and white mica indicates the microfold axial planes (Fig. 7b).

The medium grade rocks are not substantially diverse from the high grade rocks in terms of petrography. Leucosome bands, however, are exclusively found in the high level rocks of the study region and may be utilized to identify them in the field (Fig. 7b).

The foliation of the medium level rocks contains epidote (Fig. 7c).

The epidote grains are easily recognized by their high relief and range in color from colorless to light green. Similar to the high level rocks, the mica foliation is overgrown by the garnets in the medium level rocks (Fig. 7d).

While K-feldspar was just noticed, plagioclase grains are distinguished from medium level rocks including anorthite and albite.

The metavolcano-sedimentary rocks are located in the Zaam and Baydah groups. The metavolcanic samples are black in color, fine-grained, and medium to high sheared in the study region (Figs. 7e, 7f).

Quartz, potash feldspars, and plagioclase are its principal constituents at the microscopic scale. These rocks have well-elongated minerals, occasionally with garnet inclusions (Fig. 7e).

Additionally, the metasedimentary rocks are sheared in a vertical dipping, N–W-trending orientation.

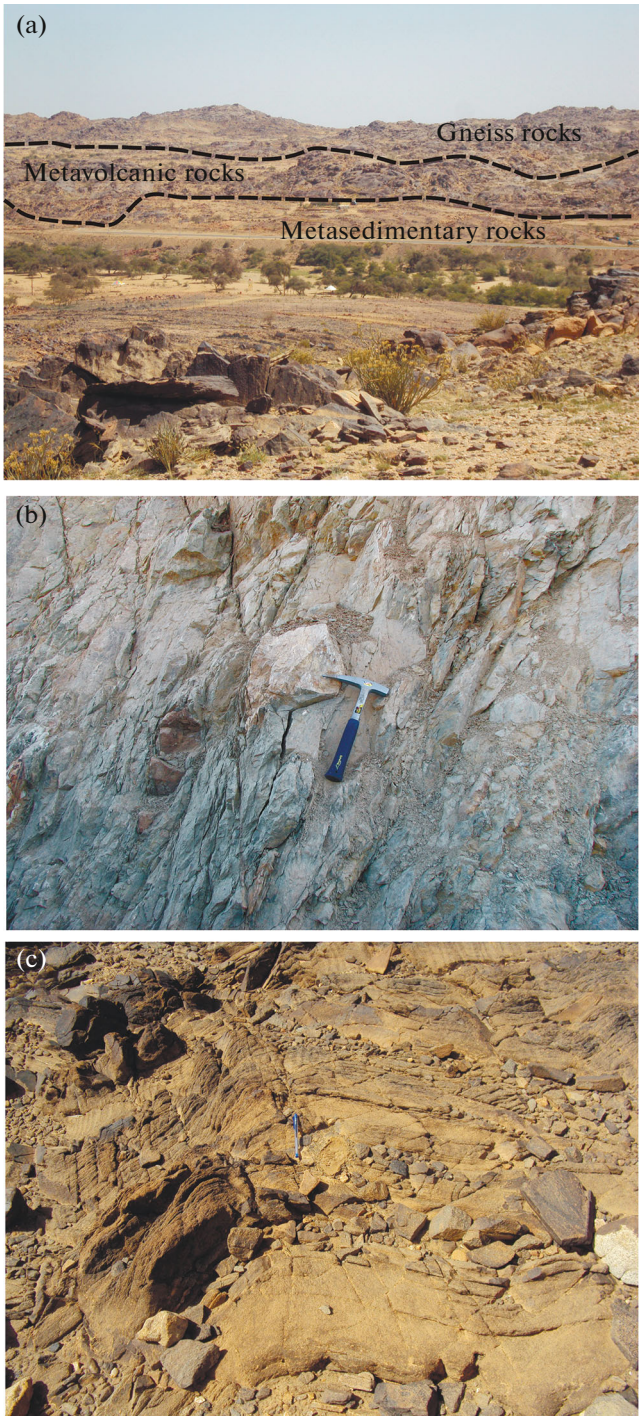

Fig. 6. (a) Field photo shows general view for tectonic contacts for various rock units; (b) decimetric photo for metavolcano-sedimentary rocks show foliation planes; (c) open-parallel folds at the zone margin to tight-flattened profiles.

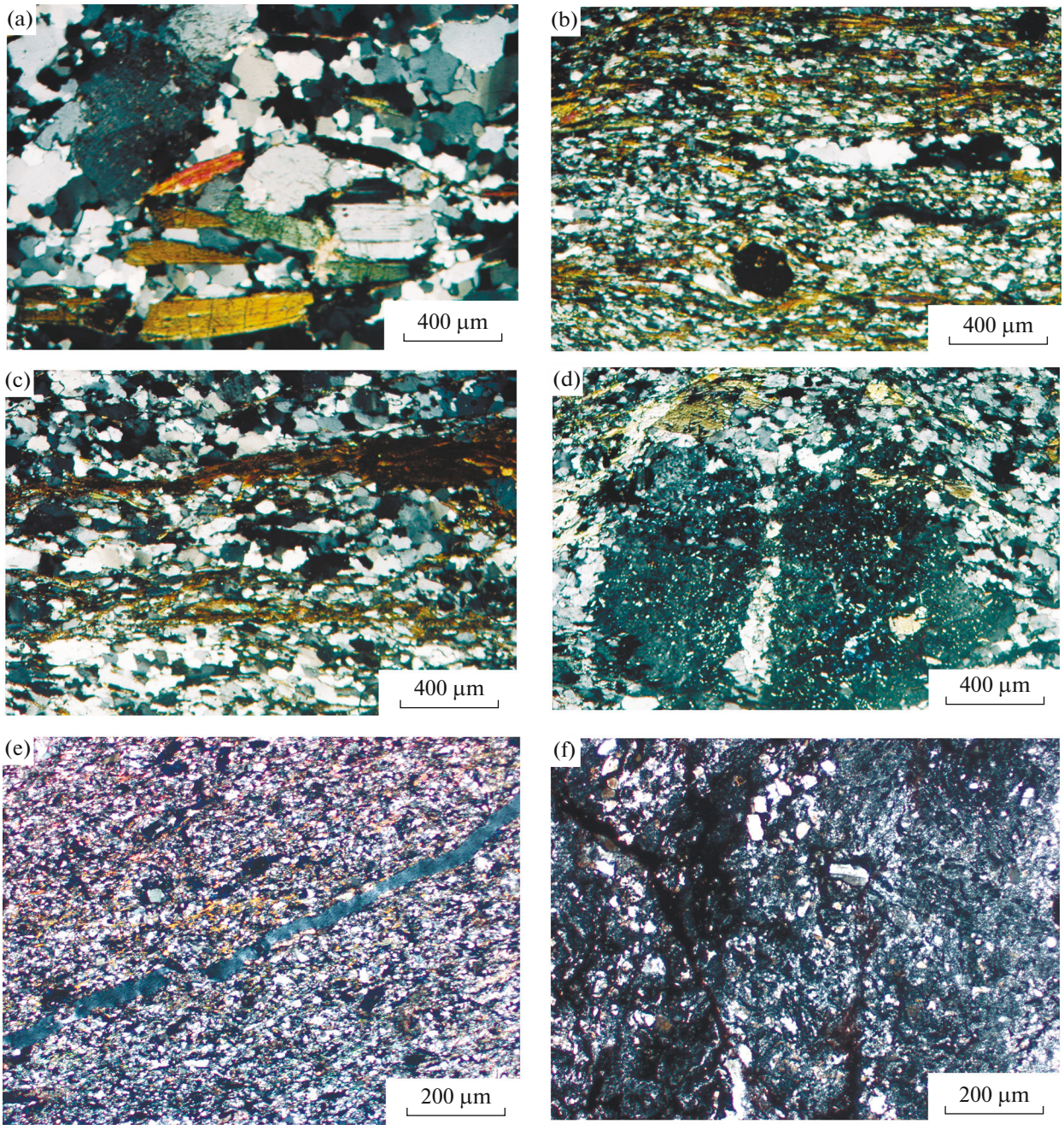

Fig. 7. (a) Microphotographs showing high grade metamorphic rocks contain feldspar, quartz, garnet, micas, chlorite, and ilmenite (Sample Ha-5); (b) foliation and lineation for gneissic rock with the microfold axial planes for biotite and white mica (Sample Ha-6); (c) the foliation of the medium grade rocks contains epidote for gneisses samples (Sample Ha-2); (d) the mica foliation is overgrown by the garnets in the medium grade rocks (Sample Ha-8); (e) the metavolcano-sedimentary rocks for the Zaam group are well-elongated minerals (Sample Za-3); (f) the metavolcano-sedimentary rocks for the Baydah group are fine-grained, and medium to high sheared (Sample Ba-2).

K-feldspar, quartz, and plagioclase make up its fine and dark-colored grains (Fig. 7e).

It appears that finely foliated and opaque minerals, with epidote acting as a minor mineral, are utilized as accessories in certain thin portions. Plagioclase may be seen breaking into K-feldspars and bending and kinking in certain thin slices, which is a faint sign of cataclastic activity (Fig. 7f).

The intrusive rocks split into three major types due to the degree of deformation: undeformed granite, deformed granodiorite, and mylonitized granite. The intruding undeformed granite shows a post-deforma-

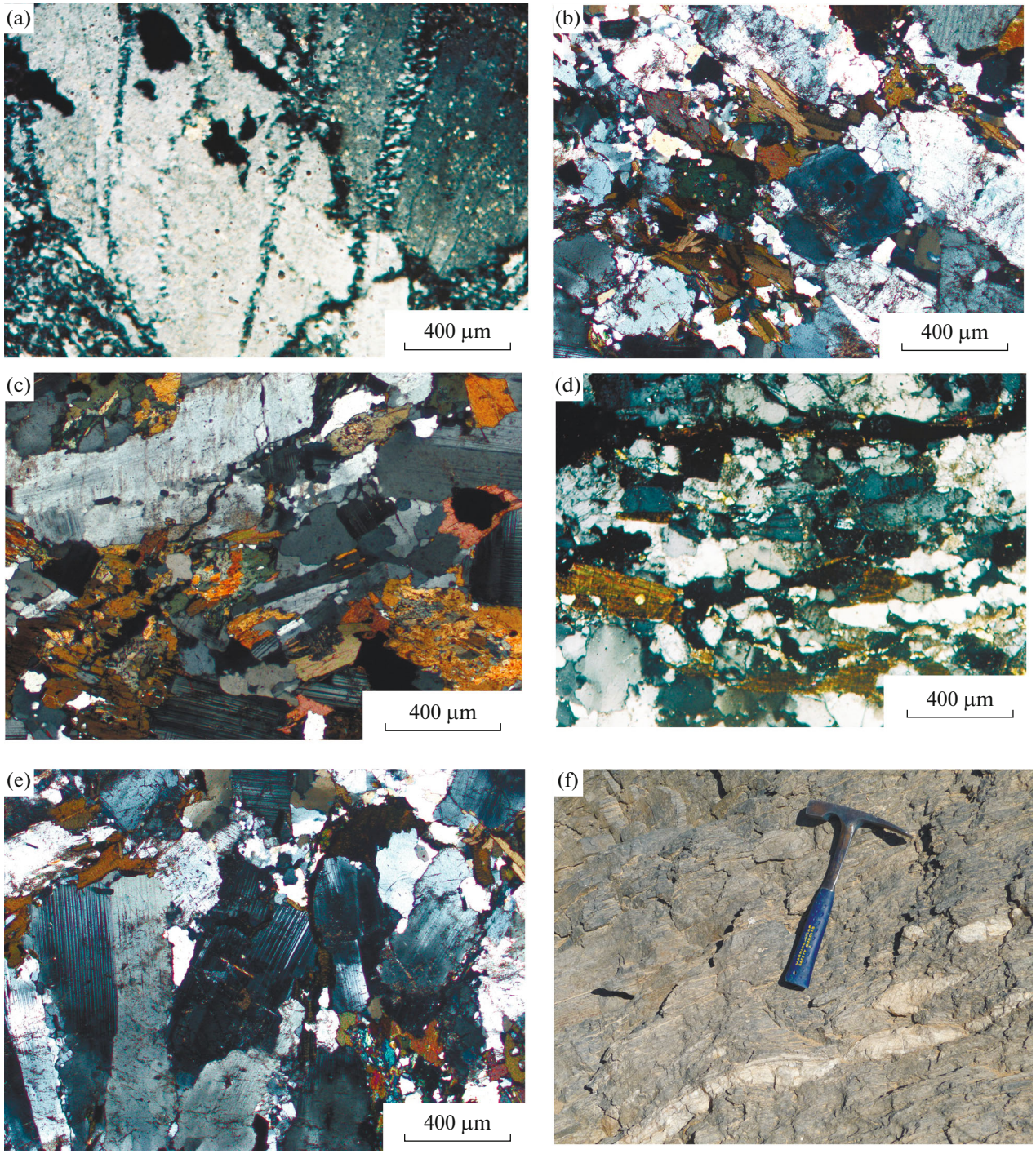

Fig. 8. (a)–(e) Microphotographs showing: (a) Undeformed granite shows and contain quartz, potash feldspars and plagioclase (Sample Q-4); (b) slightly granite has alkali feldspar, plagioclase, quartz and mafic minerals (Sample Q-1); (c) mylonitic granite are contained elongated quartz aggregates and biotite (Sample Q-3); (d) deformed granodiorite displays plagioclase, quartz, hornblende (Sample Jar-3); (e) the deformed granodiorite is medium sheared with medium to coarse grained (Sample Jar-2); (f) field photograph exhibits that mylonitized granite rocks with numerous quartz stringers and feldspar augen with elliptical-shaped.

tion cross-cutting interaction between it and the shear zone for deformed rocks (Fig. 8a).

The undeformed granite typically has microperthite of alkali feldspar, plagioclase, quartz, biotite and hornblende. It is also homogeneous, coarse grains, equigranular that is porphyritic in certain localized areas (Fig. 8b).

The mylonitized granite rocks exhibit numerous quartz stringers and feldspar augen with elliptical-shaped (Fig. 8c).

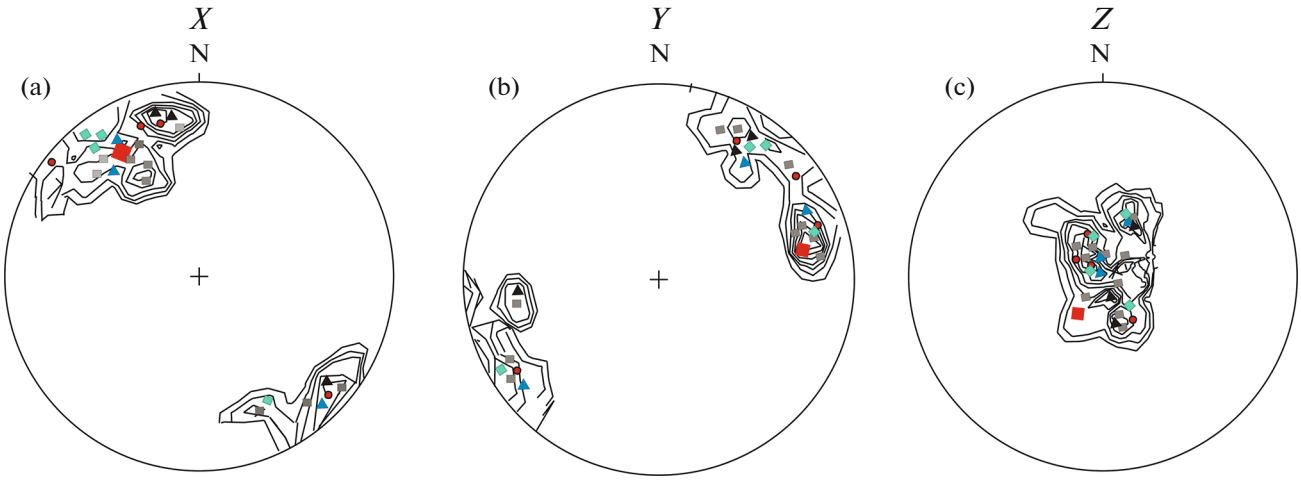

Fig. 9. Lower hemisphere for equal area projections for 24 collected samples showing: (a) Maximum extension direction (*X*); (b) intermediate direction (*Y*); (c) maximum shortening direction (*Z*). Contours start at 3% and increment every 5%; red squares in the stereographic projections represent mean values of tensor averages. Gneiss rocks are shown by grey squares; metavolcano-sedimentary rocks from the Zaam group are red circle; metavolcano-sedimentary rocks from Baydah group are blue triangle; granodiorite rocks are black triangle; Qazzaz Granite rocks are green rhombus.

It is described by the augen of K-feldspar or asymmetrical porphyroclasts and plagioclase with blastomylonitic texture. The mylonitic granite are contained elongated quartz aggregates and biotite with fine to medium grains in matrix (Fig. 8d).

Deformed granodiorite displays a number of intrusive bodies with compositions ranging from tonalite to granodiorite. These bodies typically form concordant contact related to the foliations for the shear zone. Although, it is difficult to see deformation in the field, it is visible only in thin sections (Fig. 8e).

The majority of the rock units are uniform, medium to coarse grains, and occasionally porphyritic. They are made of quartz, plagioclase, hornblende and biotite and also contain a bimodal grains size distribution. Zircon, opaque minerals, and epidote are examples of accessory minerals (Fig. 8f).

FINITE STRAIN RESULTS

Direction of Finite Strain

The strain measurements reveal that in the Hamadat core complex, the long axes (*X*-axes) of the finite strain grains trend NW to SE with tiny dips for gneisses rocks, metavolcano-sedimentary rocks from the Zaam and Baydah groups, granodiorite for the Jar-Salajah, and Qazzaz granite (Fig. 9).

The mean value for the long axis for different lithologies is found to be clustering along a NW to SE trending with 10°dip. The intermediate direction (*Y*-axis) is also represented in figure 9 with E/ENE and W/WSW directions and medium dip. The mean value for different lithologies exhibits the NE/SW trending and plunging around 35°.

Additionally, it is subvertical behavior for the *X* direction. The subhorizontal foliation is parallel to the maximum shortening direction (*Z*-axis), which steeply plunges to the WSW/ENE trending (Fig. 9). The maximum contoured data (*Z*-axis) is 200°/65°.

Strain Symmetry

The Flinn diagram depicts the strain results, which we summarized [11] (Fig. 10, Table 1). The relative strain ellipsoids shape such as prolate versus oblate, is crucial for identifying the strain type, for example, constructional versus flattening. The strain ellipsoids show oblate strain symmetry (Fig. 10).

The "K" value is shown to be the strain symmetry in the various lithologies and to identify the tectonic contacts in the Hamadat core complex [44]. It ranges from 0.05 to 0.65 for the Rf/φ technique and from 0.02 to 0.76 for the Fry technique [17] (Tabl. 1). Because of this, the strain measurements in the Hamadat core complex indicate oblate strain symmetry for gneisses rocks, metavolcano-sedimentary rocks from the Zaam and Baydah groups, granodiorite for the Jar-Salajah, and Qazzaz granite (Figs. 10a, 10b).

The Fry strain results are roughly more than the Rf/φ strain results and do not differ significantly for different rock units, proving that there is no visible difference between the two sets of observations. The bulk of the samples that were assessed appeared to be flattening (Fig. 10).

According to the Rf/φ and Fry techniques, the stenches *X*-axes (S_X) and strain symmetry (*K*) display a favourable association (Figs. 11a, 11b).

However, there is also a negative link between the strain symmetry (*K*) and the stenches *Y*-axis (S_Y) (Figs. 11c, 11d).

Additionally, there is no obvious correlation and typically continuous relationship between the strain symmetry (*K*) and the stenches *Z*-axis (S_Z) (Figs. 11e, 11f).

Also we provided strain data that was used to create the Flinn diagram to help visualize our findings (Figs. 10, 11).

Finite Stretches

The strain values for gneisses rocks, metavolcano-sedimentary rocks, granodiorite and Qazzaz granite in the Hamadat core complex was displayed (Table 1). According to the Rf/φ method, the axial ratio (*XZ* section) ranges from:

— 2.20 to 4.5 for gneisses rocks;

— 1.90 to 2.10 for Zaam group metavolcano-sedimentary rocks;

— 1.80 to 2.10 for Baydah group metavolcano-sedimentary rocks;

— 2.00 to 2.30 for Jar-Salajah granodiorite;

— 1.90 to 2.10 for Qazzaz granite.

As well, S_X sections for gneisses rocks, metavolcano-sedimentary rocks vary from (Table 1):

— 1.61 to 2.24 (gneiss rocks);

— 1.36 to 1.72 (Zaam groups metavolcano-sedimentary rocks);

— 1.59 to 1.76 (Baydah group metavolcano-sedimentary rocks);

— 1.38 to 1.65 (Jar-Salajah granodiorite);

— 1.28 to 1.48 (Qazzaz granite).

Using the Fry approach, the axial ratios (*XZ*) for different rock units range from 3.30 to 7.40, 2.50 to 3.40, 2.90 to 3.50, 2.40 to 3.60 and 2.10 to 2.60, respectively.

Additionally, S_X sections range from (Table 1):

— 1.65 to 2.26 for gneisses rocks;

— 1.42 to 1.74 for metavolcano-sedimentary rocks from the Zaam group;

— 1.67 to 1.80 for metavolcano-sedimentary rocks from the Baydah group;

— 1.35 to 1.42 for granodiorite rocks;

— 1.30 to 1.43 for Qazzaz granite rocks.

Stretches (Sz) for the Rf/φ method in all examined samples range from 0.31 to 0.64, suggesting a vertical shortening of 36 to 69%. Stretches (Sz) using the Fry procedure vary from 0.29 to 0.62, indicating vertical shortening of 38 to 71% for gneisses rocks, metavolcano-sedimentary rocks from the Zaam and Baydah groups, granodiorite, and Qazzaz granite. In addition, the S_Y ranges for the Rf/φ and the Fry methods were 1.06 to 1.52 and 1.04 to 1.60, respectively (Table 1).

Our analysis shows that the stretching axis of both approaches is comparable. The strain records a little difference in the deformation behavior between both approaches, in addition to the similar deformation in the different lithologies. The measured samples demonstrate that there is no discernible difference in the deformation attitude of various rocks. Additionally, under the metamorphic conditions, the analyzed samples suffered equal deformation of the strain magnitude. Therefore, the most crucial step of foliation is the mode of deformation throughout all lithologies (Figs. 12, 13).

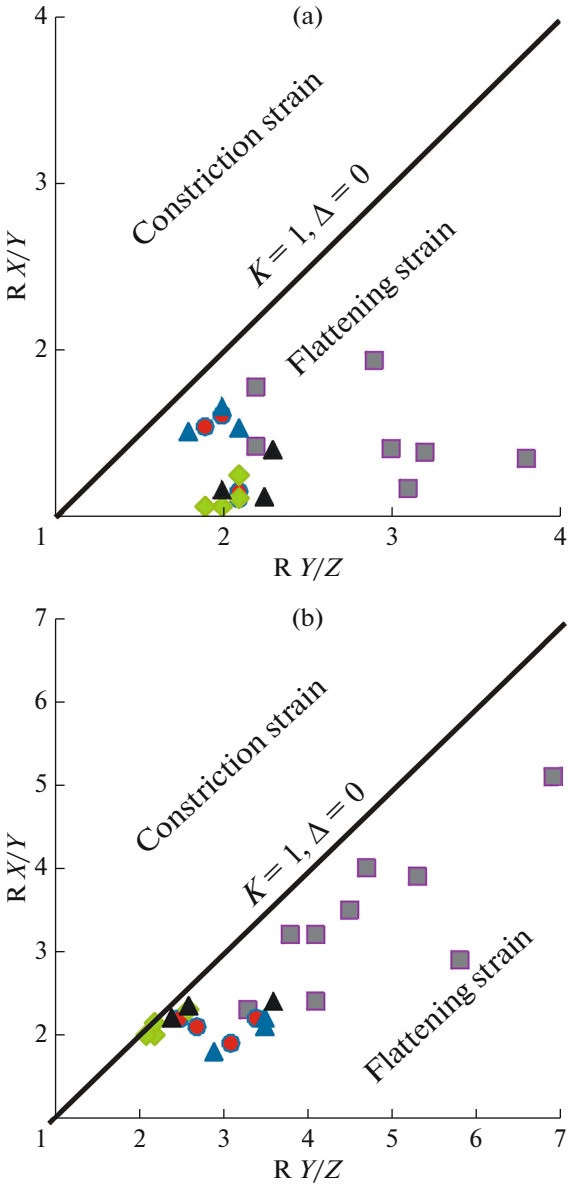

Fig. 10. Flinn diagram ([11]) for strain symmetry: (a) Rf/φ method; (b) Fry method. Gneiss rocks are shown by grey squares, metavolcano-sedimentary rocks from the Zaam group are red circle; metavolcano-sedimentary rocks from Baydah group are blue triangle, granodiorite rocks are black triangle; Qazzaz Granite rocks are green rhombus.

Strain Magnitude

The Nadai parameter referred to as the strain magnitudes for samples of gneisses rocks, metavolcano-sedimentary rocks from the Zaam and Baydah groups,

Table 1. Finite strain data for collected samples from Hamadat core complex

Sample No.	Rock type	Method	*Rxy*	*Ryz*	*Rxz*	Stretch			Principal strain Ratios	Radius	Strain magnitude	Lode`s parameter	Log*X*/*Y*	Log*Z*/*Y*	Ln*X*/*Y*	Ln *Y*/*Z*
						Sx	*Sy*	*Sz*	*K*	*R*	*Et*					
Ha-1	Gneiss	Rf/φ	1.41	2.20	3.10	1.63	1.16	0.53	0.34	2.61	0.820	0.394	0.15	–0.34	0.34	0.79
		Fry	1.43	2.30	3.30	1.68	1.17	0.51	0.33	2.73	0.866	0.395	0.16	–0.34	0.36	0.83
Ha-2	Gneiss	Rf/φ	1.16	3.10	3.60	1.61	1.39	0.45	0.08	3.26	0.990	0.767	0.06	–0.49	0.15	1.13
		Fry	1.19	3.20	3.80	1.65	1.39	0.43	0.09	3.39	1.027	0.743	0.07	–0.51	0.17	1.16
Ha-3	Gneiss	Rf/φ	1.38	3.20	4.40	1.82	1.33	0.41	0.17	3.58	1.103	0.570	0.14	–0.51	0.32	1.16
		Fry	1.29	3.50	4.50	1.80	1.40	0.40	0.11	3.79	1.139	0.666	0.11	–0.54	0.25	1.25
Ha-4	Gneiss	Rf/φ	1.34	3.80	5.10	1.90	1.41	0.37	0.12	4.14	1.228	0.639	0.13	–0.58	0.29	1.34
		Fry	1.36	3.90	5.30	1.93	1.42	0.36	0.12	4.26	1.255	0.632	0.13	–0.59	0.31	1.36
Ha-5	Gneiss	Rf/φ	1.40	3.00	4.20	1.80	1.29	0.43	0.20	3.40	1.061	0.531	0.15	–0.48	0.34	1.10
		Fry	1.28	3.20	4.10	1.74	1.36	0.42	0.13	3.48	1.065	0.649	0.11	–0.51	0.25	1.16
Ha-6	Gneiss	Rf/φ	1.77	2.20	3.90	1.91	1.07	0.49	0.64	2.97	0.966	0.159	0.25	–0.34	0.57	0.79
		Fry	1.71	2.40	4.10	1.91	1.12	0.47	0.51	3.11	1.007	0.241	0.23	–0.38	0.54	0.88
Ha-7	Gneiss	Rf/φ	1.93	2.90	5.60	2.21	1.15	0.39	0.49	3.83	1.229	0.236	0.29	–0.46	0.66	1.06
		Fry	2.00	2.90	5.80	2.26	1.13	0.39	0.53	3.90	1.252	0.240	0.30	–0.46	0.69	1.06
Ha-8	Gneiss	Rf/φ	1.39	4.90	6.80	2.11	1.52	0.31	0.10	5.29	1.450	0.658	0.14	–0.69	0.33	1.59
		Fry	1.35	5.10	6.90	2.11	1.56	0.31	0.05	5.45	1.469	0.687	0.13	–0.71	0.30	1.63
Ha-9	Gneiss	Rf/φ	1.20	4.10	4.90	1.80	1.51	0.37	0.06	4.30	1.231	0.776	0.08	–0.61	0.18	1.41
		Fry	1.18	4.00	4.70	1.77	1.50	0.38	0.06	4.18	1.203	0.792	0.07	–0.60	0.17	1.39
Ha-10	Gneiss	Rf/φ	1.58	4.50	7.10	2.24	1.42	0.32	0.17	5.08	1.451	0.535	0.10	–0.65	0.46	1.50
		Fry	1.35	5.50	7.40	2.15	1.60	0.29	0.08	5.85	1.528	0.703	0.13	–0.71	0.30	1.70
Za-1	Metavolcano-sedimentry	Rf/φ	1.10	2.10	2.30	1.36	1.24	0.59	0.09	2.20	0.646	0.782	0.04	–0.39	0.10	0.74
		Fry	1.14	2.20	2.50	1.42	1.25	0.57	0.11	2.34	0.702	0.721	0.06	–0.34	0.13	0.79
Za-2	Metavolcano-sedimentry	Rf/φ	1.14	2.10	2.40	1.40	1.22	0.58	0.13	2.24	0.667	0.695	0.06	–0.32	0.13	0.74
		Fry	1.29	2.10	2.70	1.51	1.18	0.56	0.26	2.39	0.730	0.494	0.11	–0.32	0.25	0.74

Table 1. (Contd.)

Sample No.	Rock type	Method	*Rxy*	*Ryz*	*Rxz*	Stretch			Principal strain Ratios	Radius	Strain magnitude	Lode`s parameter	Log*X*/*Y*	Log*Z*/*Y*	Ln*X*/*Y*	Ln *Y*/*Z*
						Sx	*Sy*	*Sz*	*K*	*R*	*Et*					
Za-3	Metavolcano-sedimentry	Rf/φ	1.60	2.00	3.20	1.72	1.08	0.54	0.60	2.60	0.828	0.192	0.20	–0.30	0.47	0.69
		Fry	1.55	2.20	3.40	1.74	1.12	0.51	0.45	2.75	0.877	0.289	0.19	–0.34	0.44	0.79
Za-4	Metavolcano-sedimentry	Rf/φ	1.53	1.90	2.90	1.64	1.08	0.57	0.58	2.43	0.758	0.206	0.18	–0.28	0.43	0.64
		Fry	1.63	1.90	3.10	1.72	1.05	0.55	0.70	2.53	0.802	0.135	0.21	–0.28	0.49	0.64
Ba-1	Metavolcano-sedimentry	Rf/φ	1.65	2.00	3.30	1.76	1.07	0.53	0.65	2.65	0.848	0.161	0.22	–0.30	0.50	0.69
		Fry	1.67	2.10	3.50	1.80	1.08	0.51	0.61	2.77	0.891	0.184	0.22	–0.32	0.51	0.74
Ba-2	Metavolcano-sedimentry	Rf/φ	1.50	1.80	2.70	1.59	1.06	0.59	0.63	2.30	0.706	0.184	0.18	–0.26	0.41	0.59
		Fry	1.61	1.80	2.90	1.67	1.04	0.58	0.76	2.41	0.754	0.104	0.21	–0.26	0.48	0.59
Ba-3	Metavolcano-sedimentry	Rf/φ	1.52	2.10	3.20	1.70	1.11	0.53	0.48	2.62	0.833	0.276	0.18	–0.32	0.42	0.74
		Fry	1.59	2.20	3.50	1.77	1.11	0.51	0.49	2.79	0.896	0.259	0.20	–0.34	0.46	0.79
Q-1	Deformed granite	Rf/φ	1.05	2.00	2.10	1.30	1.24	0.62	0.05	2.05	0.587	0.868	0.02	–0.30	0.05	0.69
		Fry	1.10	2.00	2.20	1.34	1.22	0.61	0.10	2.10	0.609	0.758	0.04	–0.30	0.10	0.69
Q-2	Deformed granite	Rf/φ	1.24	2.10	2.60	1.48	1.19	0.57	0.22	2.34	0.709	0.553	0.09	–0.32	0.22	0.74
		Fry	1.13	2.30	2.60	1.43	1.27	0.55	0.10	2.43	0.735	0.743	0.05	–0.35	0.12	0.83
Q-3	Deformed granite	Rf/φ	1.05	1.90	2.00	1.28	1.22	0.64	0.06	1.95	0.546	0.852	0.02	–0.28	0.05	0.64
		Fry	1.05	2.00	2.10	1.30	1.24	0.62	0.05	2.05	0.587	0.868	0.02	–0.30	0.05	0.69
Q-4	Undeformed granite	Rf/φ	1.10	2.10	2.30	1.36	1.24	0.59	0.09	2.20	0.646	0.782	0.04	–0.32	0.10	0.74
		Fry	1.02	2.15	2.20	1.31	1.28	0.60	0.02	2.17	0.635	0.942	0.01	–0.33	0.02	0.77
Jar-1	Deformed granodiorite	Rf/φ	1.11	2.25	2.50	1.41	1.27	0.56	0.09	2.36	0.709	0.770	0.05	–0.35	0.10	0.81
		Fry	1.11	2.35	2.60	1.42	1.29	0.55	0.08	2.46	0.742	0.788	0.04	–0.37	0.10	0.85
Jar-2	Deformed granodiorite	Rf/φ	1.15	2.00	2.30	1.38	1.20	0.60	0.15	2.15	0.631	0.664	0.06	–0.30	0.14	0.69
		Fry	1.09	2.20	2.40	1.38	1.26	0.57	0.08	2.29	0.682	0.801	0.04	–0.34	0.09	0.79
Jar-3	Deformed granodiorite	Rf/φ	1.39	2.30	2.20	1.65	1.18	0.51	0.30	2.69	0.848	0.432	0.14	–0.36	0.33	0.83
		Fry	1.50	2.40	3.60	1.35	1.17	0.49	0.36	2.90	0.926	0.367	0.18	–0.38	0.41	0.88

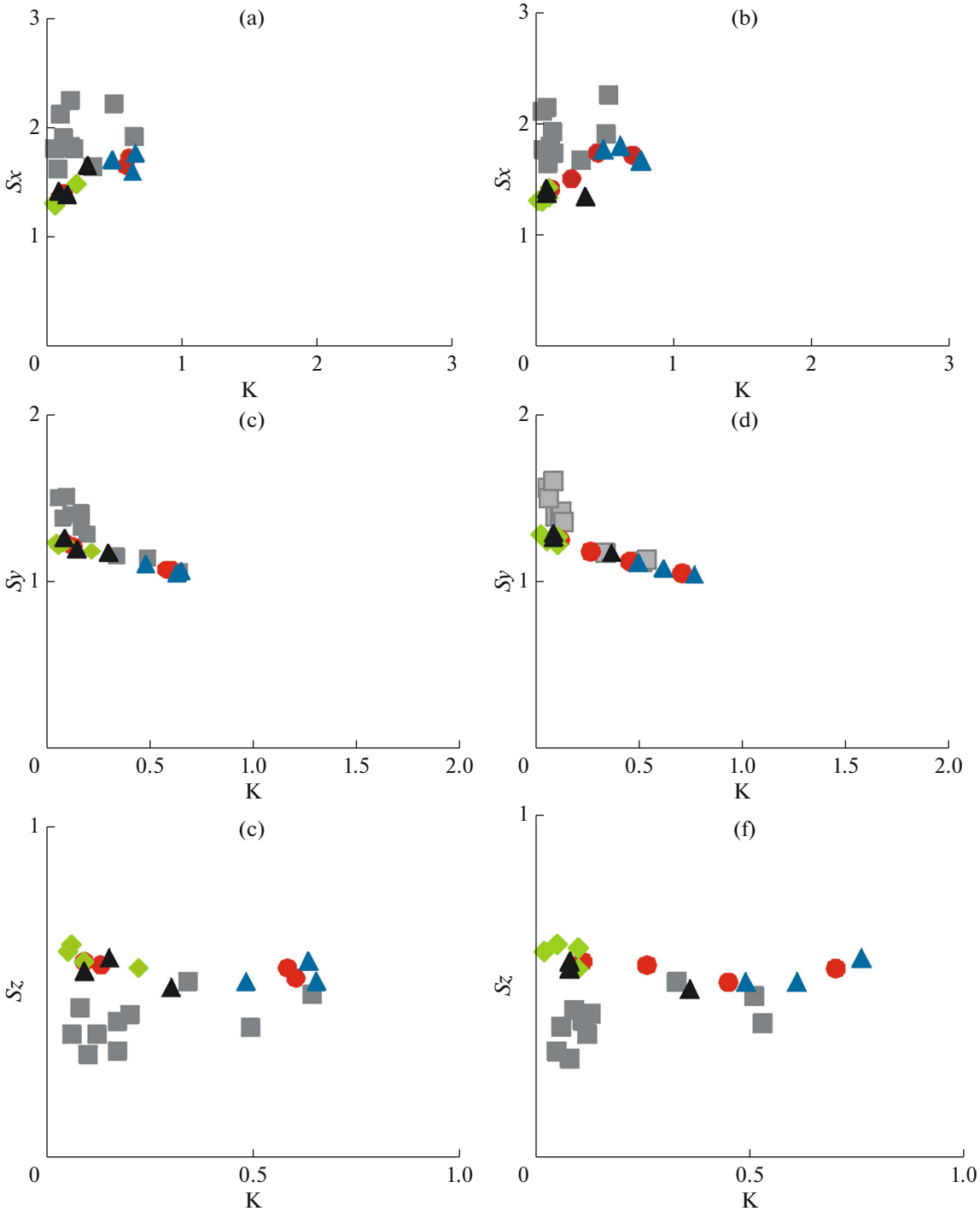

Fig. 11. Flinn diagram ([11]) showing relative strain or strain symmetry: (a) *SX* vs. *K* showing a positive correlation for Rf/φ method; (b) *SX* vs. *K* showing a positive correlation for Fry method; (c) *SY* vs. *K* showing a pronounced negative correlation for Rf/φ method; (d) *SY* vs. *K* showing a pronounced negative correlation for Fry method; (e) *SZ* vs. *K* showing no obvious correlation for Rf/φ method. (f) *SZ* vs. *K* showing no obvious correlation for Fry method. Gneiss rocks are shown by grey squares, metavolcano-sedimentary rocks from the Zaam group are red circle; metavolcano-sedimentary rocks from Baydah group are blue triangle; granodiorite rocks are black triangle; Qazzaz Granite rocks are green rhombus.

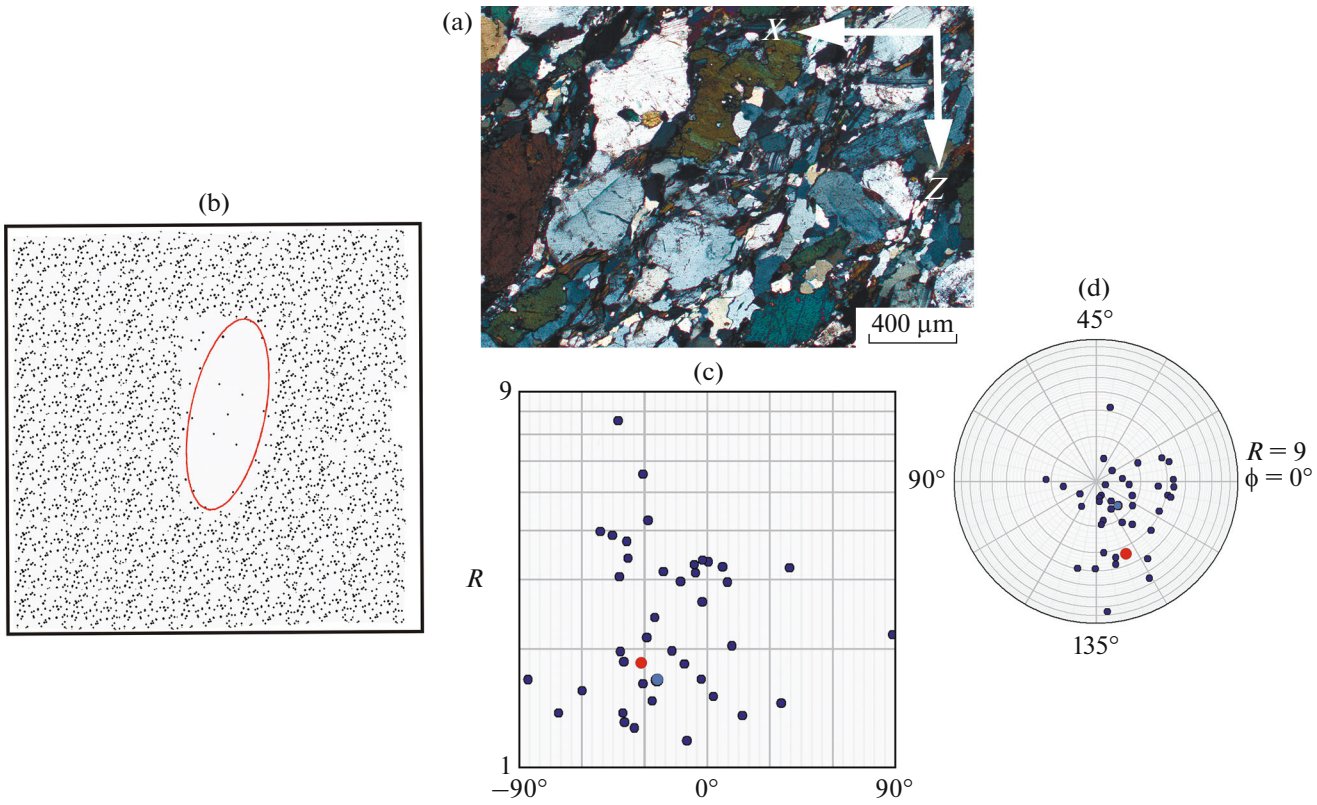

Fig. 12. For *XZ*: (a) Micrograph; (b) Center to center graph; (c) Rf/phi graph; (d) Polar graph (for *XZ* plane at sample Ha-7). Measured grains (blue dots); mean value for grains (red dot).

granodiorite, and Qazzaz granite in the Hamadat core complex. The strain magnitudes are depended on the Lode shape for the rate of strain ellipsoids (Fig. 14).

According to [38], the chart displayed a plot based on the circle 60° sector. The Lode factor can be identified by varying the direction of radial line in accordance with the magnitude factor that has been measured [44].

For the Rf/ and Fry techniques, the examined strain magnitude samples range from 0.546 to 1.451 and from 0.587 to 1.528, respectively (Table 1).

The obtained data are heterogeneous deformation. Additionally, the strain magnitude indicates that increased with the reduction of the Lode's factor in various rocks. In the current area, the strain magnitude also identified the impact of structural contact and strain intensity (Fig. 14).

Volume Deformation

The strain ellipsoid shape revealed the strain type and exposed constrictional and flattening form, as well as the volume strain. High grade rocks may show minute volume changes throughout the deformation [25, 35]. The logarithmic strain graph was created by [53] to show the volume change and accompanying deformation. The ln Y/Z and ln X/Y values are shown on an $X-Y$ chart for the logarithmic strain graph (Fig. 15, Table 1).

The real flattening and constriction producing from volume losses for the deformation are divided by $\Delta = 0\%$, $\Delta = 20\%$, and $\Delta = 40\%$, respectively, according to the straight-line logarithmic strain graph.

The measured samples for gneisses rocks, metavolcano-sedimentary rocks from the Zaam and Baydah groups, granodiorite, and Qazzaz granite in the Hamadat core complex are represented as flattened ellipsoids. Additionally, for ellipsoids, the volume loss varies between 0 and 40% (Fig. 15).

DISCUSSION

Several arc-terranes create the Arabian Nubian Shield. The boundaries of these terranes are clearly delineated, somewhere arc-continental and arc–arc sutures split them [21].

According to [2], ophiolitic and serpentinites identify the sutures.

Arc–arc accretions were a multistage development that resulted in successive overprinting of the tectonic evidence of the earlier steps, according to evidence from the Arabian–Nubian Shield [3].

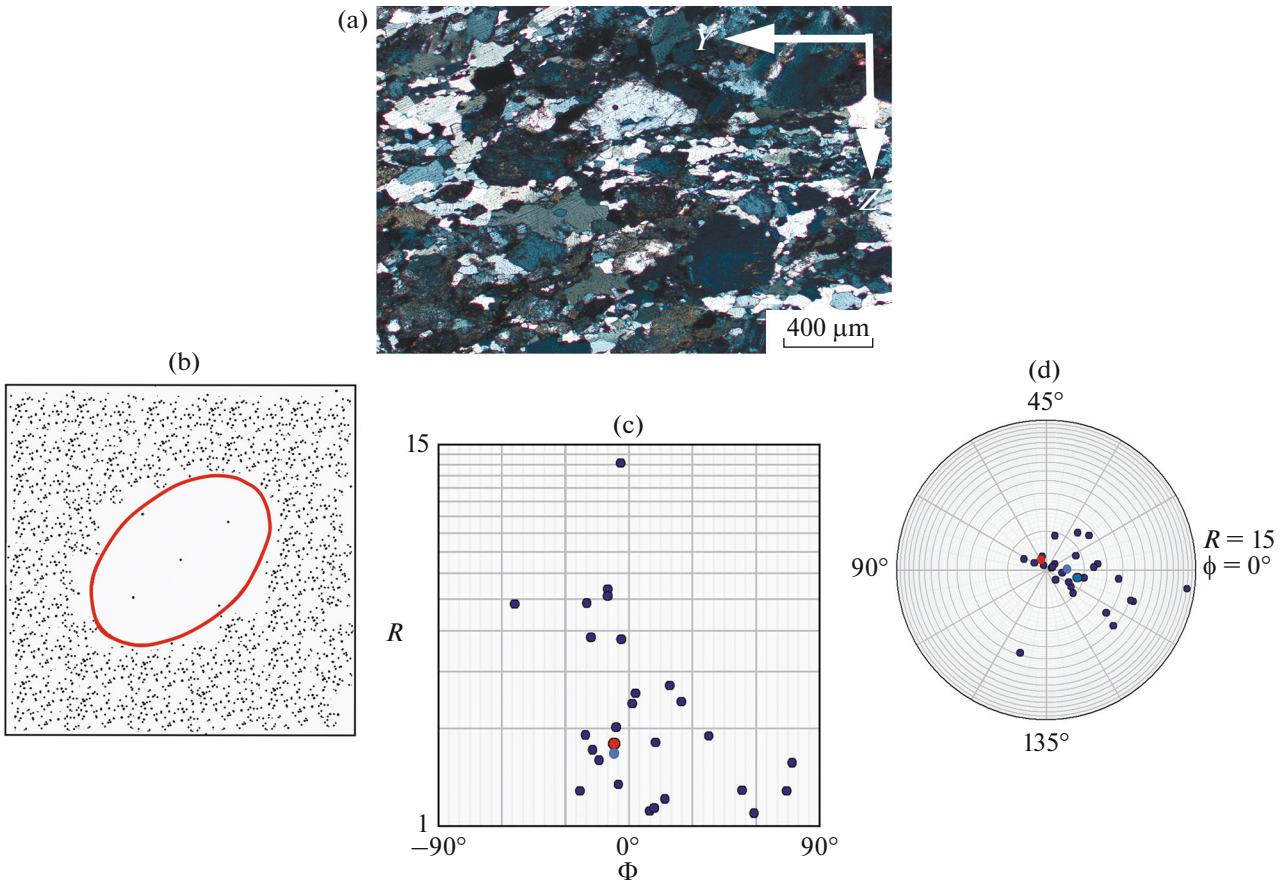

Fig. 13. For *YZ*: (a) Micrograph; (b) Center to center graph; (c) Rf/phi graph; (d) Polar graph (for *YZ* plane at sample Ha-7). Measured grains (blue dots); mean value for grains (red dot).

The Yanbu suture divided into the Hijaz terrain (in the south) and the Midyan terrain (in the north) [1]. There were four deformation stages in the research region, with the first and two deformations ENE–WSW to E–W shortening times being associated to the subduction and collision phase between the Hijaz and Midyan terranes [18, 19]. The third deformation is associated with an oblique transpression control with left-lateral progress, whereas the fourth deformation time partly evolved as thrust lines between the intrusion of granitic and the surrounding rocks.

It is not well known how the polarity of the subduction changed during the first and two events collision occurrences between the Hijaz and Midyan terranes. But the study of dipping thrust planes on SE to S/SE suggested that the Midyan terrain may have subducted below the Hijaz terrain [21].

The most NW of these terranes are represented the Midyan terrane. It also contains metavolcano-sedimentary and intrusion rocks with volcanic rocks and later molasse sediments. The Najd fault system is a massive shear zone that trends NW–SE direction [47].

Early shear for the Najd fault system was ductile and took place in the depths with an amphibolite facies. Brittle shearing occurred in the shallow strata of this system [13, 21].

The high-grade metamorphic complexes as Hamadat complexes were found in the Midyan terrane beside large-strands of the Najd system that comprise the three shear zones (Qazzaz, Ajjaj, and Hanabiq regions). The majority of the metamorphic complexes have NW–SE trend, or parallel to the direction of shear zones [2].

The Najd fault system is visible throughout much of the Arabian–Nubian shield. However, space imagery [41] reveals that the Ajjaj–Qazzaz–Hamadat regions are its mainly spectacular sector, explaining a variety of timing associations related to intrusion rocks [18, 19].

The NW–SE direction branches of the Najd Fault System's shear zones display left-lateral shear, whereas related N–S and NE–SW striking directions exhibit right-lateral movement. The all different units create a network of planar anastomoses that distinguished a huge with less deformed fish-shaped parts [15].

The N–S trend for Hanabiq shear zone is a branch of the Ajjaj shear zone. Inside the Ajjaj shear zone, the Hamadat complex is a exhumed of gneiss dome. Both

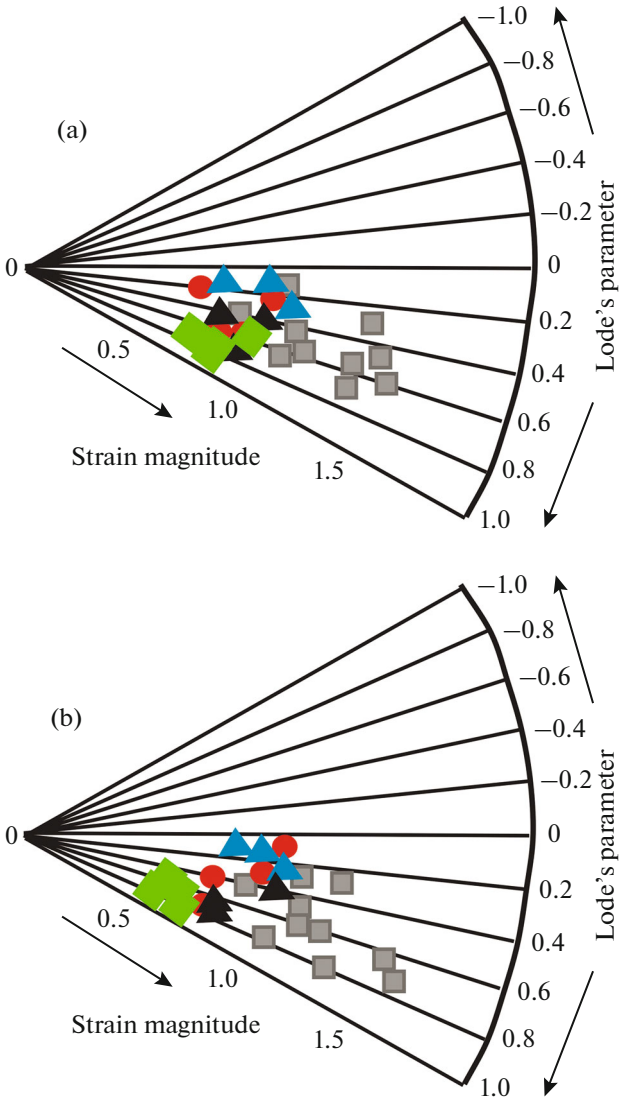

Fig. 14. Nadai's diagram vs. Lode's parameter for the the Hamadat core complex region (a) refer to Rf/φ methods and (b) refer to Fry methods. Gneiss rocks are show by grey squares; metavolcano-sedimentary rocks from the Zaam group are red circle; metavolcano-sedimentary rocks from Baydah group are blue triangle; granodiorite rocks are black triangle; Qazzaz Granite rocks are green rhombus.

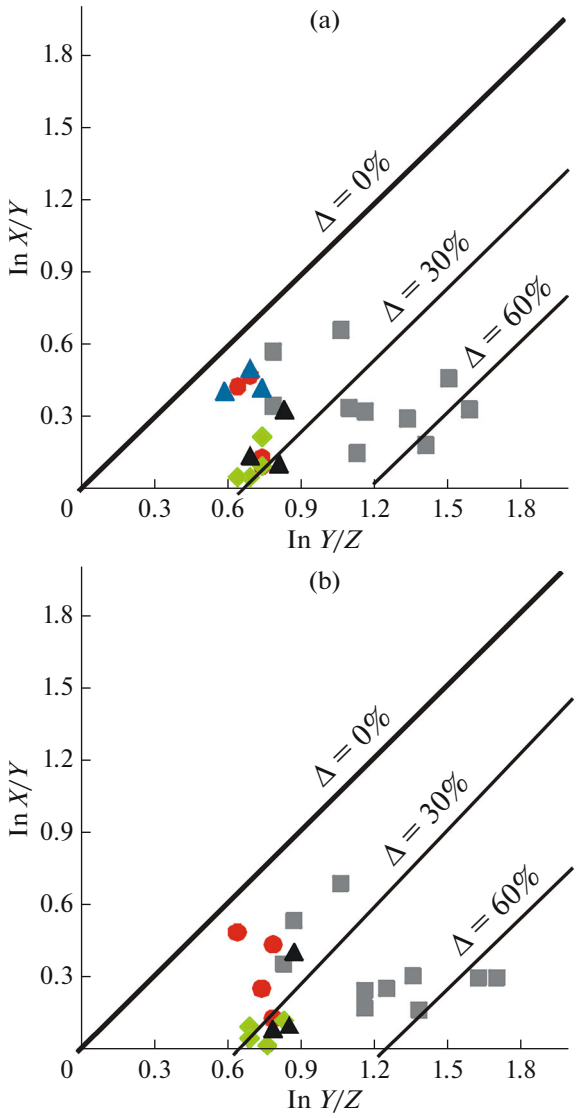

Fig. 15. Logarithmic strain diagram; Straight lines characterized the plane strain for 0, 20, and 40% volume loss; [$K = \ln(X/Y)/\ln(Y/Z)$]. (a) refer to Rf/φ and (b) refer to Fry method. Gneiss rocks are show by grey squares, metavolcano-sedimentary rocks from the Zaam group are red circle, metavolcano-sedimentary rocks from Baydah group are blue triangle, granodiorite rocks are black triangle, and Qazzaz Granite rocks are green rhombus.

intrusive and metamorphic rocks form the Hamadat complex.

Researchers [18, 19] utilized the intrusive rocks to restrict the Ajjaj shear zone activity to activity based on their various cross cutting connections to the shear zone.

In the current study, the Hamadat core complex shows gneisses, metavolcano-sedimentary rocks from the Zaam and Baydah groups, granodiorite, and Qazzaz granite. These metamorphic rocks contain garnet, muscovite, biotite, feldspar, and quartz, which represented the peak of metamorphism. The garnet porphyroblasts are characterized by invading the foliation that post-deformational conditions were satisfied for peak metamorphism. Additionally, the Hamadat core complex activity terminated before the chlorite created, static retrograde chlorite appears to be overprinting the peak metamorphic assemblages [18, 19, 37].

The lineations in the Hamadat core complex that are trending northwest to southeast are also connected to kinematic markers that demonstrate this direction of tectonic movement. In this instance, we found that the subhorizontal main phase foliations controls tectonic background in the study region.

For different lithologies, the main phase foliations run parallel to subparallel to the tectonic contact. Based on the strain measurements, the axial ratios (*XZ*) in the

various rocks in the Hamadat core complex exhibit metamorphism rocks from medium to high strains.

In the present results, the nappe structure was heterogeneously deformation under ductile strain. Additionally, the current region highlights the substantial strain accumulation that was caused by tectonic movements at the strike slip fault [5, 31].

Our study suggested that if the high grade rocks porosities stay extremely low through deformation, relatively small or no volume changes may be envisaged [35]. The Hamadat core complex displays oblate strain symmetry, according to the strain measurements.

In addition to pure shearing, vertical shortening also contributed to the development of ductile deformation during sinistral shear. There is no clear pattern for the "K" value, which represents the strain type. It is indicated how the significant amount exhibits the flattening strain as a result of vertical shortening, which was connected to thrusting of the study area.

Therefore, we proposed that the nappe contacts were shaped by growth overthrusting through brittle to ductile conditions before metamorphism and deformation. It was discovered that the subhorizontal foliation in the examined area contributed to the vertical shortening. The vertical shortening is in conjunction with pure shear due to the subhorizontal foliation under investigation area [6, 45].

The ductile feldspar is produced as a result of the thrusting-stimulated deformation for the Rf/φ and fry strains. It showed that the pre-existing structures remained in low strain regions between shear zones due to exceptionally high strain. Furthermore, it demonstrated how thrusting and intrusions cause deformation times with finite strain accumulations via brittle to ductile deformations. The nappe contacts and sinistral shear indicators in the Hamadat core complex were caused by the single deformational event, according to the conclusions of the strain data.

CONCLUSIONS

Our research results leads to the summary of the finite strain and deformation data for the Hamadat core complex region.

(1) The different rocks such as gneisses, metavolcano-sedimentary from the Zaam and Baydah groups, granodiorite, and Qazzaz granite for the Hamadat core complex region were subjected to the same deformation events at around the same events.

(2) Our results showed flattening strain type and oblate strain symmetry in the Hamadat core complex region. Additionally, it concluded that during thrusting and intrusions throughout the deformation process, and building of brittle to ductile deformation was mostly caused by pure shearing in studied area.

(3) It concluded that the shortening axes are subvertical related to the subhorizontal foliations. The strain data have the same main-phase foliation and similar deformation behaivour. Finite strain acquired all through high pressure metamorphism in this instance suggests that the nappe boundaries developed during the buildup of ductile strain and, consequently, brittle strain through the intrusions.

ACKNOWLEDGMENTS

The authors are grateful to the financial support received from the Researchers Supporting Project no. (RSPD2024R781), King Saud University, Riyadh, Saudi Arabia. The authors are grateful to reviewers for useful comments and Editor M.N. Shoupletsova (GIN RAS, Moscow, Russia) for careful editing.

FUNDING

The research performed was supported by Researchers Supporting Project no. (RSPD2024R781), King Saudi University, Riyadh, Saudi Arabia.

CONFLICT OF INTEREST

The authors of this work declare that they have no conflicts of interest.

REFERENCES

1. M. G. Abdelsalam, M. M. Abdeen, H. M. Dowidar, R. J. Stern, and A. A. Abdelghaffar, "Structural evolution of the Neoproterozoic western Allaqi–Heiani Suture Zone, Southern Egypt," Precambrian Res. **124**, 87–104 (2003).
2. M. G. Abdelsalam and R. J. Stern, "Sutures and shear zones in the Arabian–Nubian Shield," J. Afr. Earth Sci. **23**, 289–310 (1996).
3. T. S. Abu-Alam and M. M. Hamdy, "Thermodynamic modelling of Sol Hamed serpentinite, south eastern desert of Egypt: Implication for fluid interaction in the Arabian–Nubian Shield ophiolites," J. Afr. Earth Sci. **99**, 7–23 (2014).
4. F. C. Adrian, S. D. Boger, and C. Fay "Constriction structures related to viscous collision, southern Prince Charles Mountains, Antarctica," J. Struct. Geol. **46**, 142–157 (2016).
5. Y. A. Al-Amri and O. M. K. Kassem, "The effect of finite strain and deformation history of Halaban area, eastern Arabian Shield, Saudi Arabia," Arab. J. Geosci. **10** (2), 1–12 (2017).
6. A. M. Al-Saleh and O. M. K. Kassem, "Microstructural finite strain analysis and 40Ar/39Ar evidence for the origin of the Mizil gneiss dome, eastern Arabian Shield, Saudi Arabia," J. Afr. Earth Sci. **70**, 24–35 (2012).
7. H. A. Al-Shanti and J. M. Abo Omar, "Effect of olive cake on layers' performance and egg quality," J. Al-Azhar Univ. Gaza (Nat. Sci.) **6** (1), (2003).
8. V. E. Camp, "Island arcs and their role in the evolution of the western Arabian Shield," GSA Bull. **95**, 913–921 (1984).

9. F. B. Davies and G. McEwen *Geologic Map of the Al Wajh Quadrangle, Sheet 26 B, Kingdom of Saudi Arabia, Map GM-83, Scale 1 : 250000* (Saudi Arabian Deputy Ministry for Mineral Resources, 1985).
10. J. L. Doebrich, A. M. Al-Jehani, A. A. Siddiqui, T. S. Hayes, Y. Saleh, J. Wooden, P. R. Johnson, F. H. Kattan, B. Shaikan, M. Basahel, H. Zahran, and A. Al-Shammari, "Geology and mineral resources of the Ar Rayn terrane, eastern Arabian Shield, Kingdom of Saudi Arabia," Precambrian Res. **158**, 17–50 (2007).
11. D. Flinn, "On folding during three-dimensional progressive deformation," Quart. J. Geol. Soc. London **118**, 385–433 (1962).
12. D. Flinn, "Construction and computation of three-dimensional progressive deformations," J. Geol. Soc. London **135**, 291–305 (1978).
13. H. Fritz, M. Abdelsalam, K. A. Ali, B. Bingen, A. S. Collins, A. R. Fowler, W. Ghebreab, C. A. Hauzenberger, P. R. Johnson, T. M. Kusky, P. Macey, S. Muhongo, and R. J. Stern, "Orogen styles in the East African Orogen: a review of the Neoproterozoic to Cambrian tectonic evolution," J. Afr. Earth Sci. **86**, 65–106 (2013).
14. N. Fry, "Random point distributions and strain measurement in rocks," Tectonophysics **60** (1–2), 89–105 (1979).
15. A. Genna, P. Nehlig, E. Le Goff, C. Guerrot, and M. Shanti "Proterozoic tectonism of the Arabian Shield," Precambrian Res. **117**, 21–40 (2002).
16. Z. Hamimi, O. M. K. Kassem, and M. N. El-Sabrouty, "Kinematic analysis technique for deformed lithologies in Al Amar suture, eastern Arabian Shield," Geotectonics **49** (5), 439–450 (2015).
17. S. S. Hanna and N. Fry, "A comparison of methods of strain determination in rocks from southwest Dyfed (Pembrokeshire) and adjacent areas," J. Struct. Geol. **1** (2), 155–162 (1979).
18. M. Hassan, T. S. Abu-Alam, C. Hauzenberger, and K. Stüwe "Geochemical signature variation of pre-, syn-, and post-shearing intrusives within the Najd fault system of western Saudi Arabia," Lithos **263**, 274–291 (2016a).
19. M. Hassan, K. Stüwe, T. S. Abu-Alam, U. Klotzli, and M. Tiepolo, "Time constraints on deformation of the Ajjaj branch of one of the largest Proterozoic shear zones on Earth: The Najd fault system," Gondwana Res. **34**, 346–362 (2016b).
20. P. R. Johnson, A. Andersen, A. S. Collins, A. R. Fowler, H. Fritz, W. Ghebrab, T. Kusky, and R. J. Stern, "Late Cryogenian–Ediacaran history of the Arabian–Nubian Shield: A review of depositional, plutonic, structural, and tectonic events in the closing stages of the northern east African orogen," J. Afr. Earth Sci. **61** (3), 167–232 (2011).
21. P. R. Johnson, *Explanatory Notes to the Map of Proterozoic Geology of Western Saudi Arabia, Techn. Rep. SGS-TR-2006-4, Scale 1 : 1500000* (Saudi Geol. Surv., 2006).
22. P. R. Johnson, G. P. Halverson, T. M. Kusky, R. J. Stern, and V. Pease, "Volcanosedimentary basins in the Arabian–Nubian Shield: Markers of repeated exhumation and denudation in the Neoproterozoic accretionary orogen," Geosciences **3**, 389–445 (2013).
23. A. Y. Kahal, E. A. El-Motaal, O. M. K. Kassem, and A. H. R. Al Ghoreiby, "Strain analysis and deformation history of Zalm area, Arabian Shield, Saudi Arabia," J. Afr. Earth Sci. **150**, 441–450 (2019).
24. O. M. K. Kassem, A. L. A. Almutairi, A. A. M. Al Bassam, and H. J. Al Faifi, "Relationship between finite strain and tectonic setting in the Ar Ruwaydah area, Eastern Arabian Shield, Saudi Arabia," Arab. J. Geosci. **9** (19), Art. 728 (2016).
25. O. M. K. Kassem, Z. Hamimi, H. Aboelkhair, A. Abdelhalim, and M. Al-Gabali "Microstructural study and strain analysis of deformed Neoproterozoic lithologies in Um Junud area, Northern Nubian Shield," Geotectonics **53** (1), 125–139 (2019).
26. O. M. K. Kassem, S. H. Abd El Rahim, and E. R. El Nashar, "Strain analysis and Microstructural evolution characteristic of Neoproterozoic rocks associations of Wadi El Falek, Centre Eastern Desert, Egypt," Geotectonics **46** (5), 379–388 (2012).
27. O. M. K. Kassem, "Kinematic vorticity technique for porphyroclasts in the metamorphic rocks: An example from the northern thrust in Wadi Mubarak belt, Eastern Desert, Egypt," Arab. J. Geosci. **5** (1), 159–167 (2012).
28. O. M. K. Kassem, "Kinematic analysis of the Migif area in the Eastern Desert of Egypt," J. Afr. Earth Sci. **90**, 136–149 (2014).
29. O. M. K. Kassem, "Strain analysis and deformation in the Tanumah Area, Arabian Shield, Saudi Arabia," Arab. J. Geosci. **8** (6), 4127–4138 (2015).
30. O. M. K. Kassem and Z. Hamimi "Finite strain analysis of Fatima shear zone in Western Arabia," Geotectonics **52** (2), 251–265 (2018).
31. O. M. K. Kassem and A. M. Al-Saleh, "Vorticity analysis and deformation history of the Mizil gneiss dome, Eastern Arabian Shield, Saudi Arabia," Geotectonics **52** (3), 346–358 (2018).
32. O. M. K. Kassem and S. Abdel Raheim, "Finite-strain analysis of the metavolcanics and metapyroclastics in gold-bearing shear zone of the Dungash area, Central Eastern Desert, Egypt," Geotectonics **48** (6), 484–497 (2014).
33. O. M. K. Kassem and Z. Hamimi "Application of finite strain technique for deformed lithologies in Al Amar suture, Eastern Arabian Shield," The Open Geol. J. **8**, Suppl. 1, 97–106 (2014).
34. O. M. K. Kassem and U. Ring, "Under plating-related finite-strain patterns in the Gran Paradiso massif, Western Alps, Italy: Heterogeneous ductile strain superimposed on a nappe stack," J. Geol. Soc. London **161**, 875–884 (2004).
35. L. M. Noman, O. M. K. Kassem, and A. M. Al Bassam, "Finite Strain analysis for deformed Neoproterozoic rock associations of the Al Amar fault zone, Eastern Arabian Shield, Saudi Arabia," Arab. J. Geosci. **13** (6), 272–288 (2020).
36. S. Meyer, C. Passchier, T.S. Abu-Alam, and K. Stüwe, "A strike-slip core complex from the Najd fault system, Arabian Shield," Terra Nova **26** (5), 387–394 (2014).
37. A. Nadai, *Theory of Flow and Fracture of Solids* (McGraw-Hill, NY, USA,1963).
38. C. Pellaton, *Explanatory Notes to the Geologic Map of the Umm Lajj Quadrangle. Sheet 25B. Kingdom of Saudi*

Arabia, Geoscience Map GM-61C, Scale 1 : 250000 (Saudi Arabian Deputy Ministry for Mineral Resources, 1982).

39. V. Pluijm and S. Marshak, *Earth structure.* An *Introduction to Structural Geology and Tectonics,* 2nd ed. (Norton & Company, Inc., NY, USA, 2004).
40. J. E. Quick, "Late Proterozoic transpression the Nabitah fault system-implications for the assembly of the Arabian Shield," Precambrian Res. **53**, 119–147 (1991).
41. J. G. Ramsay, *Folding and Fracturing of Rocks* (McGraw-Hill, NY–London. 1967).
42. J. G. Ramsay and D. S. Wood, "The geometric effects of volume change during deformation processes," Tectonophysics **16**, 263–277 (1973).
43. J. G. Ramsay and M. Huber, *The Techniques of Modern Structural Geology.* Vol. 1: *Strain Analysis* (Acad. Press, London, UK, 1983).
44. U. Ring and O. M. K. Kassem, "The nappe rule: Why does it work?" J. Geol. Soc. Am. **164**, 1109–1112 (2007).
45. C. Simpson and D. G. De Poar, "Strain and kinematic analysis in general shear zones," J. Struct. Geol. **15**, 1–20 (1993).
46. R. J. Stern, "The Najd fault system, Saudi Arabia and Egypt: A Late Precambrian rift-related to transform system," Tectonics **4**, 497–511 (1985).
47. R. J. Stern and P. R. Johnson, "Continental lithosphere of the Arabian Plate: A geologic, petrologic, and geophysical synthesis," Earth-Sci. Rev. **101**, 29–67 (2010).
48. J. R. Vail, "Pan-African crustal accretion in northeast Africa," J. Afr. Earth Sci. **1**, 285–294 (1983).
49. Vollmer, Vol. 2 (2010). http://www.frederickvollmer.com/ellipsefit/index.html.
50. F. K. Zaidi, A. M. Al-Bassam, O. M. K. Kassem, H. J. Alfaifi, and S. M. Alhumidan, "Factors influencing the major ion chemistry in the Tihama coastal plain of southern Saudi Arabia: Evidences from hydrochemical facies analyses and ionic relationships," Environ. Earth Sci. **76**, Art. 472 (2017). https://doi.org/10.1007/s12665-017-6817-0
51. F. K. Zaidi, O. M. K. Kassem, A. M. Al-Bassam, and S. Al-Humidan, "Factors governing groundwater chemistry in Paleozoic sedimentary aquifers in an arid environment; a case study from Hail Province in Saudi Arabia," Arab. J. Sci. Engineer. **40** (7), 1977–1985 (2015).
52. LANDSAT images. https://landsat.visibleearth.nasa.gov/ (Accessed 2020).
53. Strain Calculator, v. 3.2. https://www.holcombe.net.au/software/straincalculator.html#download (Accessed June, 2010).